Room temperature nanocavity laser with interlayer excitons in 2D heterostructures

Liu, Yuanda; Fang, Hanlin; Abdullah Rasmita; Zhou, Yu; Li, Juntao; Yu, Ting; Xiong, Qihua; Zheludev, Nikolay; Liu, Jin; Gao, Weibo

2019

Liu, Y., Fang, H., Abdullah Rasmita, Zhou, Y., Li, J., Yu, T., . . . Gao, W. (2019). Room temperature nanocavity laser with interlayer excitons in 2D heterostructures. Science Advances, 5(4), eaav4506-. doi:10.1126/sciadv.aav4506

https://hdl.handle.net/10356/106424

https://doi.org/10.1126/sciadv.aav4506

OPTICS

Room temperature nanocavity laser with interlayer excitons in 2D heterostructures

Yuanda Liu[1,2]*, Hanlin Fang[3]*, Abdullah Rasmita[1], Yu Zhou[1], Juntao Li[3], Ting Yu[1], Qihua Xiong[1], Nikolay Zheludev[1,2,4]†, Jin Liu[3]†, Weibo Gao[1,2]†

Atomically thin layered two-dimensional (2D) materials have provided a rich library for both fundamental research and device applications. Bandgap engineering and controlled material response can be achieved from artificial heterostructures. Recently, excitonic lasers have been reported using transition metal dichalcogenides; however, the emission is still the intrinsic energy bandgap of the monolayers. Here, we report a room temperature interlayer exciton laser with MoS_2/WSe_2 heterostructures. The onset of lasing was identified by the distinct kink in the "L-L" curve and the noticeable spectral linewidth collapse. Different from visible emission of intralayer excitons in monolayer components, our laser works in the infrared range, which is fully compatible with the well-established technologies in silicon photonics. Long lifetime of interlayer excitons relaxes the requirement of the cavity quality factor by orders of magnitude. Room temperature interlayer exciton lasers might open new perspectives for developing coherent light sources with tailored optical properties on silicon photonics platforms.

INTRODUCTION

Investigations of two-dimensional (2D) layered materials have attracted substantial attention in recent years because of their novel electronic and optical properties as compared to traditional 3D bulk materials (*1*). The surface of 2D layers is free of dangling bonds, and different layers of 2D materials can be stacked together to form heterostructures with van der Waals forces (*2*, *3*). This largely eases the conventional "lattice mismatch" issue and provides even richer platforms because the properties of these van der Waals heterostructures can be engineered by the material types, lattice alignment, and coupling strengths of different layers.

Among them, one particular type is the heterostructures with transition metal dichalcogenide (TMDC) materials. Unlike graphene, monolayer TMDCs are direct bandgap materials (*4*, *5*), and their excitons can be used for light-emitting applications. To list only a few, light-emitting diodes (*6*–*8*), photon detectors (*9*), field-effect transistors (*10*), and opto-valleytronic devices (*11*) have been demonstrated. Furthermore, quantum yield for photoluminescence (PL) of TMDCs allows them to act as gain media to produce monolayer excitonic lasers, as demonstrated in several pioneering works recently (*12*–*15*). Different from monolayer TMDC intralayer excitons, heterostructures formed by these materials can emit light with interlayer excitons (*16*, *17*), with electron and holes separated in different TMDC layers (*18*). Indirect exitons in TMDC heterostructures represents one type of bandgap engineering, and the emission can cover a more flexible wavelength range.

Here, we demonstrate the first nanocavity laser based on van der Waals heterostructures. Figure 1A presents a 3D schematic of our nanolaser device, and Fig. 1B shows the optical microscope image of the real device. A van der Waals MoS_2/WSe_2 heterostructure has been chosen to play the role of the gain medium on a vertically coupled, free-standing photonic crystal cavity (PhCC). We have specially designed the cavity structure such that the field maximum is in excellent spatial overlap with the gain medium (details shown in note S1). The designed nanocavity facilitates efficient funneling of spontaneous emission from the van der Waals gain material into the cavity mode.

RESULTS

WSe_2 and MoS_2 monolayers were mechanically exfoliated from bulk single crystals onto the polydimethylsiloxane (PDMS) stamps, followed by stacking onto the cavity consecutively with a dry transfer method. The monolayers were identified and selected by using a combination of optical contrast (Fig. 1B), PL, and Raman spectroscopy (fig. S1). As shown in Fig. 1C, the intralayer exciton recombination in MoS_2 and WSe_2 monolayers results in PL peaks at about 668 and 750 nm, respectively. For MoS_2/WSe_2 heterostructures with AA stacking, a new PL peak centering at 1128.6 nm has been observed (Fig. 1C), which we attribute to the indirect excitonic emission. Several different samples have been measured to confirm the indirect exciton energy, which agrees well with previously reported results measured with scanning tunneling spectroscopy (*19*). As shown in Fig. 1D, when an indirect exciton is coupled to the cavity, a sharp cavity mode in the emission spectrum was observed with wavelength located at ~1122 nm, corresponding to the designed cavity mode of the PhCC. From Fig, 1D, we can also see that the silicon emission wavelength (1097.5 nm) is shorter than that of indirect excitons, implying that silicon has a larger bandgap, leading to a minimum absorption of indirect exciton emission, and therefore serves as an ideal cavity material for our infrared laser.

Next, we proceed to prove the lasing behavior of our device. One of the laser properties is that emission intensity in the cavity mode will increase faster when the pump power is above the lasing threshold. First, we investigate the lasing behavior at a cryo-temperature of ~5K. Figure 2A presents the evolution of the PL spectrum as a function of the excitation power around the lasing threshold. To more clearly see the spontaneous emission, here we collect with a multimode fiber in contrast to Fig. 1D of single-mode fiber collection. The broad emission spectrum corresponds to the spontaneous emission of indirect excitons. With the increase of the excitation power, the

[1]Division of Physics and Applied Physics, School of Physical and Mathematical Sciences, Nanyang Technological University, Singapore, Singapore. [2]The Photonics Institute and Centre for Disruptive Photonic Technologies, Nanyang Technological University, Singapore, Singapore. [3]State Key Laboratory of Optoelectronic Materials and Technologies, School of Physics, Sun Yat-sen University, Guangzhou 510275, China. [4]Optoelectronics Research Centre, University of Southampton, Southampton, UK.
*These authors contributed equally to this work.
†Corresponding author. Email: nzheludev@ntu.edu.sg (N.Z.); liujin23@mail.sysu.edu.cn (J. Liu); wbgao@ntu.edu.sg (W.G.)

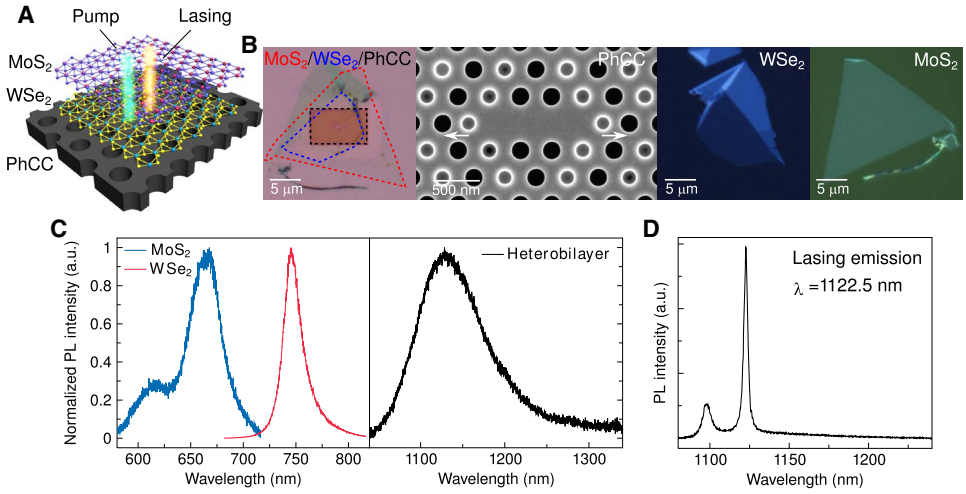

Fig. 1. MoS_2/WSe_2 heterobilayer-PhCC nanolaser. (**A**) 3D schematic image of the fabricated heterobilayer-PhCC nanolaser. (**B**) First panel: Optical microscope image of MoS_2/WSe_2 heterobilayer on silicon PhCC. The MoS_2 monolayers, WSe_2 monolayers, and PhCC are indicated by the red, blue, and black dashed lines, respectively. Second panel: Top-view scanning electron micrograph around the defect region of the L3-type defect silicon PhCC. The arrows show the displacement of the two end-holes by 0.163*a* (48.4 nm). The radius of other gray holes is shrunk to be ~62.4 nm to enhance the far-field vertical coupling. Third and fourth panels: Optical microscope image of WSe_2 and MoS_2 monolayers on PDMS before transfer, respectively. (**C**) Interlayer excitonic emission in MoS_2/WSe_2 heterobilayer compared with the intralayer emission in the two constituents. The spectra of monolayers were measured at room temperature with an excitation of 532 nm, and the spectrum of heterobilayer was measured at 5 K with an excitation of 740 nm. a.u., arbitrary units. (**D**) Cavity lasing mode emission spectrum taken at a continuous-wave pump power of 190 μW (T = 5 K). Lasing action occurs at λ = 1122.5 nm with a measured linewidth of ~2.7 nm.

cavity mode becomes more apparent as compared to the background. The experimental data can be Lorentzian fitted with a lasing peak component and a spontaneous emission component, as shown in Fig. 2B. Figure 2C exhibits their emission intensity as a function of excitation power, which is referred to as the "light input–light output" or "L-L" curve. When the excitation intensity exceeds a certain value (threshold), we can observe the rapid increase of cavity emission intensity, indicating that stimulated emission starts taking place in our device. In contrast, no kink signature was observed from the power-dependent data for spontaneous emission.

Another figure of merit for lasing is the linewidth narrowing behavior. The inset in Fig. 2D exhibits that the spectral linewidth of the cavity mode decreases gradually as the excitation power increases. The linear plot of linewidth [full width at half maximum (FWHM)] values as a function of the pump power displays a pronounced kink and plateau in the linewidth trace. The linewidth narrows by ~7%, that is, from ~2.85 to ~2.65 nm.

More evidence of lasing can be obtained from the coherence time versus pump power measurement; the coherent length was measured using a free-beam Michelson interferometer, as shown in fig. S2. The retroreflector was mounted on a linear stage to generate delay between two optical paths. The typical result of this measurement for an input power of 250 μW is shown in Fig. 3. As shown in Fig. 3B, on the basis of the raw data of intensity versus path delay, we extract the visibility as a function of path delay (Fig. 3B). Here, the visibility is defined as $\frac{I_{max}(\Delta\tau) - I_{min}(\Delta\tau)}{I_{max}(\Delta\tau) + I_{min}(\Delta\tau)}$, where $I_{max(min)}(\Delta\tau)$ is the maximum (minimum) intensity of the envelope function at a delay Δτ. We can see that the visibility contains two components: a broad component from the lasing mode contribution and a narrow component from the nonlasing mode contribution. Double Gaussian fitting is used to extract these two contributions. The coherence time of the lasing mode was extracted from the FWHM of the visibility versus path delay data. Pump power dependence of coherence time is shown in Fig. 3C. It can be seen that the coherence time reaches a saturation limit of 1.7 ps at ~35 μW, which is close to the lasing threshold obtained from the L-L curve. Notably, a saturation limit of 1.7 ps is agreeable with the coherence time derived from the laser linewidth (~1.9 ps).

The rather soft turn-on shoulder near the threshold implies a large β factor, which is defined as the ratio of the spontaneous emission coupled into the laser cavity mode over the total spontaneous emission from the material. Therefore, β factor is a measure of the optical efficiency of a laser. Its theoretical limit is unity, corresponding to the case of thresholdless lasing. We estimated the β value by fitting the log-log plot of the L-L curve to the theoretical graph on the basis of classical laser rate equations (Fig. 2E). The solid red curve is the best fit to the experimental data, yielding a β value of 0.17. Figure 2E also shows theoretical curves of β = 0.1, β = 0.4, and β = 1 as a reference. On the basis of the fitting of the L-L curve to the rate equation model, we extract a lasing threshold of ~33 μW. More detail of the theoretical model and fitting method can be found in notes S4 and S5.

The quality (Q) factor was estimated to be ~423 from $Q = \lambda/\Delta\lambda$, where Δλ is the FWHM (~2.65 nm) of the spectral cavity emission peak just above the threshold. It is worth mentioning that interlayer excitons have a much longer lifetime (~ns) as compared to the intralayer exciton (~ps). This actually largely relaxes the cavity requirement for the lasing. Our cavity Q factor above is much lower than that for the previously reported intralayer exciton lasers (*12*–*15*), but lasing can still happen here. This is mainly because of the longer lifetime of the interlayer exciton. It can be shown that, for the same cavity quality, longer carrier lifetime will result in a lower lasing threshold. We have included more detailed discussion in note S5.

Owing to the large exciton binding energy in 2D materials, high-performance lasing behavior of our device is well sustained even at room temperature. Figure 4A shows the lasing spectrum and the spontaneous emission measured at room temperature (295 K) when

the excitation spot moves on and away from the cavity. The first mode peak is located at ~1128 nm, which is red shifted by about 8 nm compared with that measured at 5 K. This comes from the energy shift of the cavity mode with varying sample temperature. Similar to the low-temperature case, a kink in the L-L curve and linewidth narrowing is observed (Fig. 4, B and C). The FWHM of the cavity mode slightly above the threshold is ~2.15 nm (Fig. 3C), which is slightly lower than that in 5 K and represents an increase of the quality factor of the cavity in room temperature. Figure 4D exhibits the log-log plot of the room temperature cavity mode intensity as a function of the pump power. The solid lines represent the simulations using standard laser rate equations. The best fit gives rise to a β factor of 0.27, signifying 10% higher coupling efficiency than that at 5 K. Lasing threshold at room temperature is estimated to be ~54 μW.

DISCUSSION

In summary, we have realized a room temperature near-infrared laser based on interlayer excitons in MoS_2/WSe_2 van der Waals heterostructures. The lasing emission was manifested by a kink feature in the L-L curve, spectral linewidth narrowing. The flexibility of heterostructures brings more possibilities in the future (*20*). Ternary phase layered material such as MoS_xSe_y or WS_xSe_y has been demonstrated to have a tunable wavelength (*21*, *22*). Vertical stacking of these materials could engineer more possible bandgaps. The wide range of 2D materials, combined with stacking orientations and different layer numbers, allows the controlled material response and shows a great promise for their nanophotonics applications. Future full integration of coherent light sources, waveguides, modulators, and detectors on single chips may eventually lead to on-chip 2D material integrated photonics (*1*, *23*).

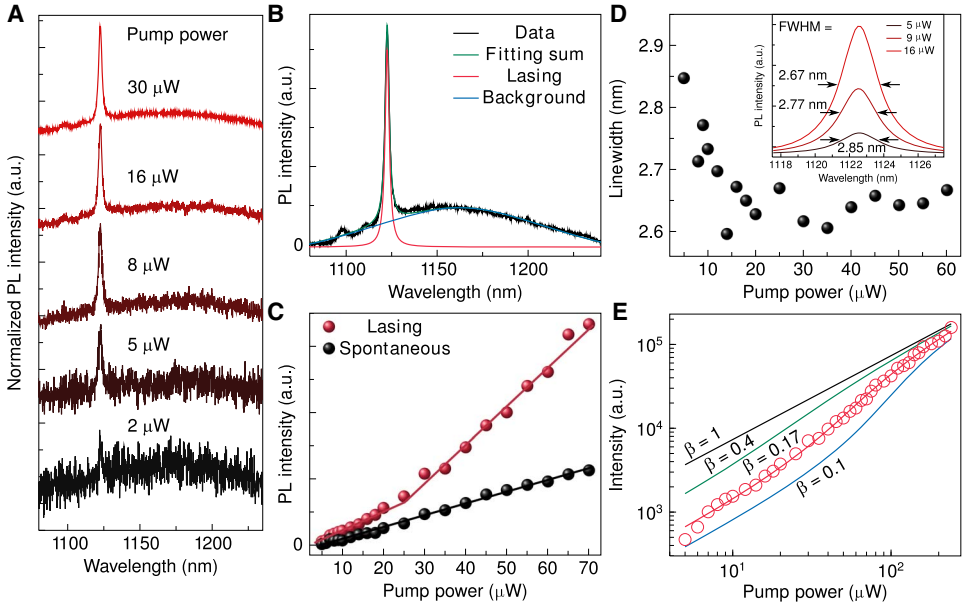

Fig. 2. Indirect excitonic lasing characteristics. (**A**) Steady-state PL emission spectra with increasing pump intensity around the threshold, illustrating the phase transition from spontaneous emission to stimulated emission. (**B**) Cavity lasing emission as compared to the heterobilayer PL background. Green line represents Lorentzian fits to the experimental data (black line), while red and blue lines represent the lasing component and background component, respectively. (**C**) L-L curve showing the output intensity at the laser wavelength as a function of the excitation pump power. The cavity mode emission (red dots) exhibits a kink, indicating the onset of superlinear emission and lasing operation, while the heterobilayer PL background emission (black dots) shows a linear dependence on the pump intensity. Solid lines are the linear fit to the experimental data. (**D**) The linewidth of the cavity mode emission as a function of the pump power. Inset: Cavity mode emission peaks with increasing pump power, exhibiting a linewidth narrowing behavior. (**E**) Log-log plot of the cavity mode emission intensity as a function of the pump power. Solid lines are the simulated results of a rate equation calculation with different β factors. Red line shows the best fit to the experimental data (red circles) corresponding to β = 0.17. The fits of 0.1, 0.4, and 1 are also shown for comparison.

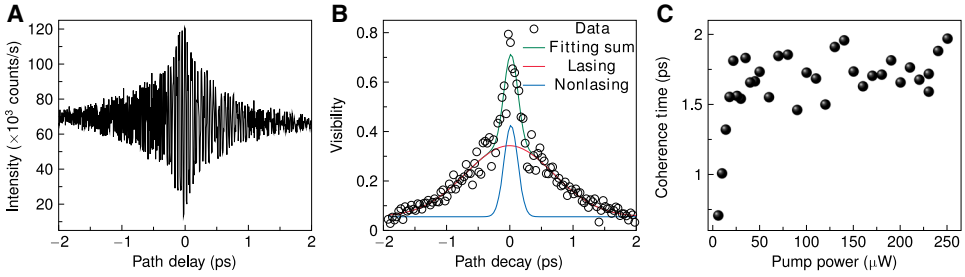

Fig. 3. Coherence time measurement. (**A**) Raw data of intensity as a function of path delay at pump power of 250 μW. (**B**) Visibility as a function of path delay at pump power of 250 μW. Two-peak Gaussian fitting is used to extract the contribution of lasing mode. (**C**) Coherence time as a function of pump power.

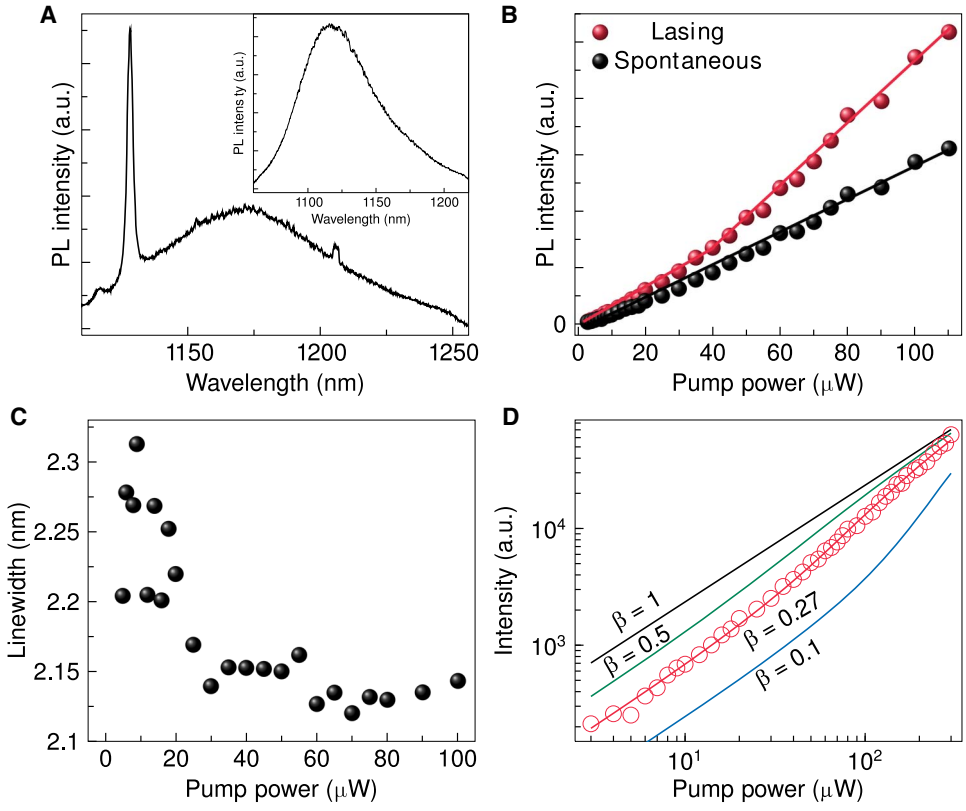

Fig. 4. Room temperature laser operation. (**A**) Room temperature cavity lasing mode emission spectrum. The linewidth is ~2.26 nm. Inset: Room temperature off-cavity spectrum of the heterobilayer for comparison. (**B**) L-L curve showing the output intensity at the laser wavelength as a function of the excitation pump power. The cavity emission exhibits a kink, indicating the onset of superlinear emission and lasing operation, while the background emission shows a linear dependence on the pump intensity. Red and black continuous lines are the linear fit to the experimental data. (**C**) Linewidth of the cavity mode emission as a function of the pump power, exhibiting linewidth narrowing profile near the threshold. (**D**) Log-log plot of the cavity mode intensity as a function of the excitation pump power. Solid lines are the simulated results of a rate equation calculation with different β factors. Red line represents the best fit to the experimental data (red circles) corresponding to β = 0.27. The fits of 0.1, 0.5, and 1 are also shown for comparison.

MATERIALS AND METHODS

Cavity design

The PhCC was fabricated from an SOI (silicon on insulator) wafer comprising a 220-nm-thick silicon layer on a 2-μm sacrificial silicon dioxide layer. The mask pattern was defined by a standard electron beam lithography process and then transferred into the silicon membrane using a hydrogen bromide–based inductively coupled plasma reactive ion etching. The silica beneath the PhCC was finally removed using a hydrofluoric acid solution to provide vertical optical isolation. This fabrication process forms an air-bridged PhCC slab with an air hole array, which produces an in-plane photonic bandgap.

Heterobilayer fabrication

WSe_2 and MoS_2 monolayers were mechanically exfoliated from bulk single crystals onto the PDMS stamps, followed by stacking onto the cavity consecutively in two dry transfer steps. The monolayers were identified and selected by using a combination of optical contrast, PL, and Raman spectroscopy. The heterobilayer was subsequently thermally annealed in a flow of forming gas ($Ar:H_2$ = 95:5 by volume) at 200°C for 3 hours.

Optical characterization

Samples were mounted on the cold head of a closed-cycle helium cryostat with variable temperature (5 K < T < 350 K). For steady-state micro-PL measurement, we excited the system with an above-bandgap (λ = 740 nm) continuous wave diode laser focused to a 1-μm spot on the surface of the sample using a 50× long working distance infrared microscope objective lens (numerical aperture = 0.65) and then positioned the laser spot onto the PhCC using piezo-electric nanopositioners. The PL signal was collected by the same objective, dispersed by a grating monochromator (300 mm^{-1}) with a spectral resolution of 0.16 nm, and detected by a liquid nitrogen–cooled charge-coupled device camera. The pumping power was adjusted using a neutral density filter.

SUPPLEMENTARY MATERIALS

Supplementary material for this article is available at http://advances.sciencemag.org/cgi/content/full/5/4/eaav4506/DC1

Note S1. PhCC design.
Note S2. Raman spectra of monolayer MoS_2 and WSe_2.
Note S3. Coherence time measurement setup.
Note S4. β Factor fitting.
Note S5. Effect of the lifetime on lasing threshold.
Fig. S1. Raman spectra of monolayer MoS_2 and WSe_2.
Fig. S2. Michelson interferometer for coherent length measurement.
Fig. S3. Illustration of the light-matter interaction.
Fig. S4. Lasing threshold versus exciton lifetime.
Fig. S5. Comparison between the PL spectrum from MoS_2/WSe_2 heterostructure and the PL spectrum from the silicon substrate.

Fig. S6. Photonic cavity characterization.
Table S1. Definition and values of the parameters used in the theoretical model.
References (*24*–*28*)

REFERENCES AND NOTES

1. F. Xia, H. Wang, D. Xiao, M. Dubey, A. Ramasubramaniam, Two-dimensional material nanophotonics. *Nat. Photonics* **8**, 899–907 (2014).
2. A. K. Geim, I. V. Grigorieva, Van der Waals heterostructures. *Nature* **499**, 419–425 (2013).
3. K. S. Novoselov, A. Mishchenko, A. Carvalho, A. H. Castro Neto, 2D materials and van der Waals heterostructures. *Science* **353**, aac9439 (2016).
4. K. F. Mak, C. Lee, J. Hone, J. Shan, T. F. Heinz, Atomically thin MoS_2: A new direct-gap semiconductor. *Phys. Rev. Lett.* **105**, 136805 (2010).
5. A. Splendiani, L. Sun, Y. Zhang, T. Li, J. Kim, C.-Y. Chim, G. Galli, F. Wang, Emerging photoluminescence in monolayer MoS_2. *Nano Lett.* **10**, 1271–1275 (2010).
6. R. S. Sundaram, M. Engel, A. Lombardo, R. Krupke, A. C. Ferrari, P. Avouris, M. Steiner, Electroluminescence in single layer MoS_2. *Nano Lett.* **13**, 1416–1421 (2013).
7. B. W. H. Baugher, H. O. H. Churchill, Y. Yang, P. Jarillo-Herrero, Optoelectronic devices based on electrically tunable p-n diodes in a monolayer dichalcogenide. *Nat. Nanotechnol.* **9**, 262–267 (2014).
8. J. S. Ross, P. Klement, A. M. Jones, N. J. Ghimire, J. Yan, D. G. Mandrus, T. Taniguchi, K. Watanabe, K. Kitamura, W. Yao, D. H. Cobden, X. Xu, Electrically tunable excitonic light-emitting diodes based on monolayer WSe_2 p–n junctions. *Nat. Nanotechnol.* **9**, 268–272 (2014).
9. O. Lopez-Sanchez, D. Lembke, M. Kayci, A. Radenovic, A. Kis, Ultrasensitive photodetectors based on monolayer MoS_2. *Nat. Nanotechnol.* **8**, 497–501 (2013).
10. B. Radisavljevic, A. Kis, Mobility engineering and a metal–insulator transition in monolayer MoS_2. *Nat. Mater.* **12**, 815–820 (2013).
11. H. Yu, G.-B. Liu, P. Gong, X. Xu, W. Yao, Dirac cones and Dirac saddle points of bright excitons in monolayer transition metal dichalcogenides. *Nat. Commun.* **5**, 3876 (2014).
12. J. Shang, C. Cong, Z. Wang, N. Peimyoo, L. Wu, C. Zou, Y. Chen, X. Y. Chin, J. Wang, C. Soci, W. Huang, T. Yu, Room-temperature 2D semiconductor activated vertical-cavity surface-emitting lasers. *Nat. Commun.* **8**, 543 (2017).
13. Y. Li, J. Zhang, D. Huang, H. Sun, F. Fan, J. Feng, Z. Wang, C. Z. Ning, Room-temperature continuous-wave lasing from monolayer molybdenum ditelluride integrated with a silicon nanobeam cavity. *Nat. Nanotechnol.* **12**, 987–992 (2017).
14. Y. Ye, Z. J. Wong, X. Lu, X. Ni, H. Zhu, X. Chen, Y. Wang, X. Zhang, Monolayer excitonic laser. *Nat. Photonics* **9**, 733–737 (2015).
15. S. Wu, S. Buckley, J. R. Schaibley, L. Feng, J. Yan, D. G. Mandrus, F. Hatami, W. Yao, J. Vučković, A. Majumdar, X. Xu, Monolayer semiconductor nanocavity lasers with ultralow thresholds. *Nature* **520**, 69–72 (2015).
16. P. Rivera, J. R. Schaibley, A. M. Jones, J. S. Ross, S. Wu, G. Aivazian, P. Klement, K. Seyler, G. Clark, N. J. Ghimire, J. Yan, D. G. Mandrus, W. Yao, X. Xu, Observation of long-lived interlayer excitons in monolayer $MoSe_2$–WSe_2 heterostructures. *Nat. Commun.* **6**, 6242 (2015).
17. H. Fang, C. Battaglia, C. Carraro, S. Nemsak, B. Ozdol, J. S. Kang, H. A. Bechtel, S. B. Desai, F. Kronast, A. A. Unal, G. Conti, C. Conlon, G. K. Palsson, M. C. Martin, A. M. Minor, C. S. Fadley, E. Yablonovitch, R. Maboudian, A. Javey, Strong interlayer coupling in van der Waals heterostructures built from single-layer chalcogenides. *Proc. Natl. Acad. Sci. U.S.A.* **111**, 6198–6202 (2014).
18. X. Hong, J. Kim, S.-F. Shi, Y. Zhang, C. Jin, Y. Sun, S. Tongay, J. Wu, Y. Zhang, F. Wang, Ultrafast charge transfer in atomically thin MoS_2/WS_2 heterostructures. *Nat. Nanotechnol.* **9**, 682–686 (2014).
19. C. Zhang, C.-P. Chuu, X. Ren, M.-Y. Li, L.-J. Li, C. Jin, M.-Y. Chou, C.-K. Shih, Interlayer couplings, Moiré patterns, and 2D electronic superlattices in MoS_2/WSe_2 hetero-bilayers. *Sci. Adv.* **3**, e1601459 (2017).
20. A. Pant, Z. Mutlu, D. Wickramaratne, H. Cai, R. K. Lake, C. Ozkan, S. Tongay, Fundamentals of lateral and vertical heterojunctions of atomically thin materials. *Nanoscale* **8**, 3870–3887 (2016).
21. S.-H. Su, W.-T. Hsu, C.-L. Hsu, C.-H. Chen, M.-H. Chiu, Y.-C. Lin, W.-H. Chang, K. Suenaga, J.-H. He, L.-J. Li, Controllable synthesis of band-gap-tunable and monolayer transition-metal dichalcogenide alloys. *Front. Energy Res.* **2**, 27 (2014).
22. A. F. Rigosi, H. M. Hill, K. T. Rim, G. W. Flynn, T. F. Heinz, Electronic band gaps and exciton binding energies in monolayer $Mo_xW_{1-x}S_2$ transition metal dichalcogenide alloys probed by scanning tunneling and optical spectroscopy. *Phys. Rev. B* **94**, 075440 (2016).
23. K. F. Mak, J. Shan, Photonics and optoelectronics of 2D semiconductor transition metal dichalcogenides. *Nat. Photonics* **10**, 216–226 (2016).
24. C. Gies, J. Wiersig, M. Lorke, F. Jahnke, Semiconductor model for quantum-dot-based microcavity lasers. *Phys. Rev. A* **75**, 013803 (2007).
25. G. Moody, C. K. Dass, K. Hao, C.-H. Chen, L.-J. Li, A. Singh, K. Tran, G. Clark, X. Xu, G. Berghäuser, E. Malic, A. Knorr, X. Li, Intrinsic homogeneous linewidth and broadening mechanisms of excitons in monolayer transition metal dichalcogenides. *Nat. Commun.* **6**, 8315 (2015).
26. M. P. van Exter, G. Nienhuis, J. P. Woerdman, Two simple expressions for the spontaneous emission factor β. *Phys. Rev. A* **54**, 3553–3558 (1996).
27. M. Kira, S. W. Koch, *Semiconductor Quantum Optics* (Cambridge Univ. Press, 2012).
28. K. Rivoire, A. Faraon, J. Vuckovic, Gallium phosphide photonic crystal nanocavities in the visible. *Appl. Phys. Lett.* **93**, 063103 (2008).

Acknowledgments

Funding: We acknowledge the support of the Singapore National Research Foundation through a Singapore 2015 NRF fellowship grant (NRF-NRFF2015-03) and its Competitive Research Program (CRP award no. NRF-CRP14-2014-02); Singapore Ministry of Education [RG119/17(s); MOE2016-T2-2-077 and MOE2016-T3-1-006 (S)]; A*Star QTE Programme, a start-up grant from NTU (M4081441); and the UK Engineering and Physical Sciences Research Council (EP/M009122/1). J. Liu and J. Li thank the support of the National Key R\&D Program of China (2018YFA0306100), the National Natural Science Foundation of China (11874437, 11761131001, 11674402, and 91750207), Guangzhou Science and Technology Project (201805010004), and the Natural Science Foundation of Guangdong (2018B030311027). Following a period of embargo, the data from this paper can be obtained from the University of Southampton ePrints research repository. **Author contributions:** W.G., J. Liu, and N.Z. conceived and supervised the project. Y.L. and Y.Z. performed experiments. H.F., J. Li, and J. Liu fabricated cavity. A.R. conceived and carried out modeling. W.G., T.Y., and Q.X., together with other authors, analyzed and discussed the results and co-wrote the manuscript. **Competing interests:** The authors declare that they have no competing interests. **Data and materials availability:** All data needed to evaluate the conclusions in the paper are present in the paper and/or the Supplementary Materials. Additional data related to this paper may be requested from the authors.

Submitted 17 September 2018
Accepted 7 March 2019
Published 26 April 2019
10.1126/sciadv.aav4506

Citation: Y. Liu, H. Fang, A. Rasmita, Y. Zhou, J. Li, T. Yu, Q. Xiong, N. Zheludev, J. Liu, W. Gao, Room temperature nanocavity laser with interlayer excitons in 2D heterostructures. *Sci. Adv.* **5**, eaav4506 (2019).